



1     **Disentangling controls of multi-scale variability in Precipitation Stable Isotopes**  
2                             **at Yadong and Ali on the Tibetan Plateau**

3     Ke Li<sup>1,2</sup>, Jing Gao<sup>1,3\*</sup>, Jingjing Yang<sup>3</sup>, Xiaowei Niu<sup>1</sup>, Aibin Zhao<sup>1</sup>, Gebanruo Chen<sup>1,2</sup>, Yuqing

4                             Wu<sup>1,2</sup>, Yigang Liu<sup>1,2</sup>

5     <sup>1</sup>State Key Laboratory of Tibetan Plateau Earth System, Environment and Resources (TPESER),

6     Institute of Tibetan Plateau Research, Chinese Academy of Sciences, Beijing, 100101, China.

7     <sup>2</sup>University of Chinese Academy of Sciences, Beijing, 100049, China

8     <sup>3</sup>Center for the Pan-Third Pole Environment, Lanzhou University, Lanzhou 730000, China

9     \* *Correspondence to:* Jing Gao (gaojing@itpcas.ac.cn)

10    **Abstract:**

11    Understanding precipitation stable isotope variability over the Tibetan Plateau (TP) is  
12    essential for identifying moisture sources and assessing climatic responses. However,  
13    drivers of daily and synoptic-scale variability beyond the westerlies and Indian  
14    Summer Monsoon (ISM) remain poorly constrained in the southern and western TP.  
15    Using event-based precipitation isotope data ( $\delta^{18}\text{O}$  and  $\delta\text{D}$ ) from Yadong and Ali  
16    (May 2021–September 2023), we investigate multi-scale variability drivers. Both sites  
17    exhibit nearly identical  $\delta^{18}\text{O}$  and  $\delta\text{D}$  magnitudes during the monsoon  
18    (June–September), while the westerly-dominated season (November–February) shows  
19    maximum differences of 12.2 ‰ in  $\delta^{18}\text{O}$  and 118.8 ‰ in  $\delta\text{D}$ . Meteorological controls  
20    vary seasonally: amount effects dominate during the monsoon ( $R = -0.28$  to  $-0.32$ ,  $p$   
21     $< 0.05$ ), while temperature effects prevail in the westerly season ( $R = 0.51$ – $0.79$ ,  $p$   
22     $< 0.001$ ). ISM dominates during isotopic convergence, while westerlies drive  
23    divergence via distinct transport pathways. Local Meteoric Water Line analysis  
24    indicates stronger moisture recycling and sub-cloud evaporation variability at Yadong.  
25    On synoptic scales, simultaneous precipitation events reflect coherent ISM influence.  
26    Interannual variability is significantly modulated by ENSO, with  $\delta^{18}\text{O}$  enrichment of  
27    2.8–5.1 ‰ from La Niña to El Niño. During El Niño, weakened Walker circulation  
28    reduces ISM transport and enhances local evapotranspiration. These results offer new  
29    constraints on seasonal moisture source transitions and reveal ENSO sensitivity



30 exceeding previous estimates, advancing understanding of atmospheric moisture  
31 transport and regional climate sensitivity over the TP.

## 32 **1 Introduction**

33 Stable oxygen and hydrogen isotopes ( $\delta^{18}\text{O}$  and  $\delta\text{D}$ ) in water are  $^{16}\text{O}$ ,  $^{17}\text{O}$ , and  $^{18}\text{O}$   
34 for oxygen, and  $^1\text{H}$  and  $^2\text{H}$  (D) for hydrogen. During water phase change, such as  
35 evaporation and condensation, isotopic fractionation leads to the change of isotopic  
36 ratios (Gat, 1996; Frankenberg et al., 2009; Yoshimura et al., 2008). Stable isotope in  
37 ice cores serve as paleothermometers (Tian et al., 2021), when interpreted through  
38 knowledge of precipitation isotope variability. Precipitation stable isotopes offer  
39 insight into moisture sources and hydrological processes and form the theoretical  
40 foundation for paleoclimate reconstruction and interpretation (Yoshimura, 2015).

41 Numerous studies have shown that precipitation isotopes are influenced by  
42 temperature, precipitation amount, and altitude (Jasechko, 2019). Additional  
43 influences include local recycling via evapotranspiration (Risi et al., 2010),  
44 convective activity (Gao et al., 2013; Risi et al., 2008), sub-cloud evaporation (Ye et  
45 al., 2024), topographic gradients (Zhang et al., 2023), atmospheric circulation (Wang  
46 et al., 2024), moisture sources (Yang and Wang, 2024), and ENSO. The linear  
47 relationship between  $\delta\text{D}$  and  $\delta^{18}\text{O}$  in precipitation, known as the Global Meteoric  
48 Water Line (GMWL;  $\delta\text{D} = 8 \times \delta^{18}\text{O} + 10$ ), was first proposed by Craig (1961). At  
49 regional scales, this is referred to as the Local Meteoric Water Line (LMWL), which  
50 varies according to local climatic conditions (e.g., temperature, precipitation amount,  
51 humidity, wind) (Gao et al., 2011), large-scale convective activity (Dansgaard, 1964),  
52 geographic factors (e.g., latitude, elevation, water recycling), and atmospheric  
53 circulation patterns (e.g., source regions and transport pathways) (Chakraborty et al.,  
54 2016). Deviations from equilibrium fractionation—such as sub-cloud  
55 evaporation—can lower both the slope and intercept of the LMWL due to the  
56 differing non-equilibrium fractionation of oxygen and hydrogen isotopes (Brunello et  
57 al., 2024). Conversely, vapor recycling tends to increase both values (Adhikari et al.,  
58 2020).



59 Deuterium excess ( $d\text{-excess} = \delta D - 8 \times \delta^{18}O$ ), introduced by Dansgaard (1964), is  
60 commonly used to assess kinetic fractionation and infer moisture source  
61 characteristics (Zhang et al., 2021). Globally, average  $d\text{-excess}$  in precipitation is  
62 around 10 ‰. Lower oceanic relative humidity during winter enhances kinetic  
63 fractionation, producing water vapor with elevated  $d\text{-excess}$  (Natali et al., 2022).

64 Isotope monitoring on the TP began in 1991 with the establishment of the Tibetan  
65 Plateau Network of Isotopes in Precipitation (TNIP) by the Chinese Academy of  
66 Sciences (Yao et al., 1991). Precipitation  $\delta^{18}O$  in the northern TP generally show  
67 positive correlation with temperature (i.e., enriched  $\delta^{18}O$  in summer, depleted in  
68 winter), while precipitation  $\delta^{18}O$  in the southern TP exhibits a negative correlation  
69 with precipitation amount, showing depletion in summer and enrichment in winter  
70 (Tian et al., 2007). Spatial precipitation  $\delta^{18}O$  patterns during summer reflect regional  
71 circulation regimes: Indian summer monsoon (ISM) dominance in the south, westerly  
72 influence in the north, and a transitional zone in central TP. In winter, westerlies  
73 dominate across the entire TP (Yao et al., 2013; Gao et al., 2009).

74 Previous studies also demonstrated that moisture origins influence precipitation  
75 isotopes (Dai et al., 2021). During monsoon seasons, convection transports marine  
76 vapor from the Bay of Bengal (BOB), Arabian Sea (AS), and Indian Ocean northward,  
77 yielding low  $d\text{-excess}$  precipitation over the Himalayas and beyond, reflecting marine  
78 vapor origins. In contrast, wintertime westerlies carry moisture from remote sources  
79 such as the Mediterranean Sea, producing precipitation with lower  $\delta^{18}O$  and elevated  
80  $d\text{-excess}$ . Local evapotranspiration contributes isotopically distinct vapor, typically  
81 enriched in both  $\delta^{18}O$  and  $d\text{-excess}$  (Noone et al., 2011; Gao et al., 2019). Local  
82 processes such as evaporation, convection, and sub-cloud evaporation also modulate  
83 isotope values seasonally: high temperatures enhance evapotranspiration and  
84 sub-cloud evaporation through unsaturated air during summer, enriching  $\delta^{18}O$ ; as  
85 sub-cloud evaporation decreases,  $d\text{-excess}$  rises (Ren et al., 2013). Vapor recycling  
86 also contributes to elevated  $d\text{-excess}$  values (Wang et al., 2016).

87 ENSO modulates precipitation across the TP by altering the Walker Circulation



88 and associated convective and large-scale moisture transport patterns (Mason and  
89 Goddard, 2001). Central Pacific El Niño events typically increase spring precipitation  
90 in the western TP and reduce it in the east, while La Niña events have the opposite  
91 effect (Wang et al., 2024). In summer, eastern Pacific El Niño events suppress rainfall  
92 in the southwest TP, while Central Pacific La Niña conditions enhance it (Liu et al.,  
93 2023). ENSO-driven changes in precipitation modify isotope signals through the  
94 amount effect, as well as upstream convective activity along vapor transport pathways.  
95 For example,  $\delta^{18}\text{O}$  values at Lhasa are significantly correlated with convective activity  
96 both in moisture source regions and along the transport path (Cai et al., 2017). ENSO  
97 also alters  $\delta^{18}\text{O}$  in the northwestern TP by affecting regional circulation patterns and  
98 the availability of water vapor (Yang et al., 2018). Therefore, the precipitation stable  
99 isotopes across the TP serve as effective tracers of ENSO-related climate variability  
100 (Murray et al., 2025).

101 The Yadong Valley, located in the southern TP within the monsoon domain,  
102 receives abundant ISM precipitation. Moisture supply linked to evaporation over  
103 northeastern India and losses associated with convection over the BoB and  
104 Bangladesh, which significantly impact  $\delta^{18}\text{O}$  and d-excess (Axelsson et al., 2023). In  
105 contrast, the Ali region in the arid western TP remains under-studied due to sparse  
106 observational data. Prior work has linked sharp mid-summer drops in  $\delta^{18}\text{O}$  to ISM  
107 intrusions, while  $\delta^{18}\text{O}$ –temperature correlations dominate during the non-monsoon  
108 season, reflecting westerly and local circulation influences (Yu et al., 2009).

109 Despite these insights, a systematic understanding of drivers on daily and  
110 synoptic-scale variability of precipitation isotopes and their response to large-scale  
111 systems such as the westerlies, ISM, and ENSO, between the southern and western TP  
112 is still lacking. Therefore, here we analyze event-based  $\delta^{18}\text{O}$  and  $\delta\text{D}$  data from Yadong  
113 and Ali (May 2021–September 2023), in conjunction with *in-situ* meteorological data,  
114 HYSPLIT backward trajectories, ERA5 reanalysis, and the Niño 3.4 index. We  
115 characterize isotope variability across daily to interannual timescales, evaluate the  
116 role of synoptic-scale moisture transport in modulating moisture sources, and assess

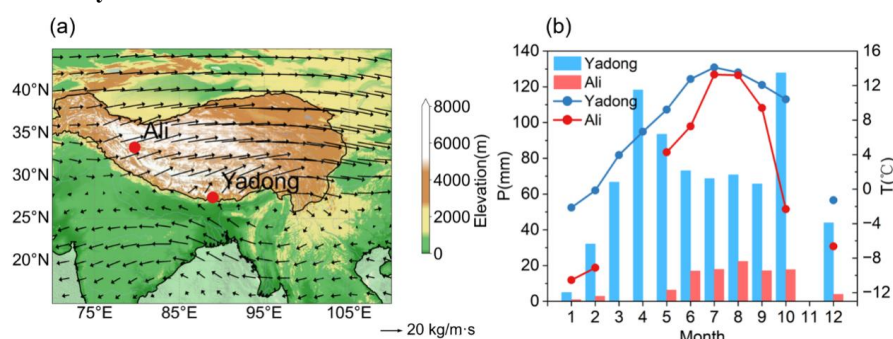


117 ENSO's impact on the TP. Our results offer new insights into precipitation isotope  
118 response to climate variations on the TP. Section 2 outlines the study sites, datasets,  
119 sampling and analysis methods. Section 3 presents the variability of precipitation  
120 isotopes and meteorological parameters, explores local controls, moisture transport  
121 process and ENSO influences on precipitation stable isotopes; and analyzes drivers of  
122 simultaneous events at Yadong and Ali.

123

## 124 2 Study Site, Data, and Methods

### 125 2.1 Study Site and Data



126

127 **Figure 1. (a) Topographic map showing the location of the Yadong and Ali study**  
128 **sites with arrows indicating the integrated water vapor flux from 500hPa to**  
129 **200hPa during the 1994 to 2023 monsoon seasons. (b) Monthly mean**  
130 **temperature (lines) and precipitation (bars) at both sites from 2021 to 2023.**

131

132 Precipitation samples were collected at Yadong and Ali sites. Yadong (88.92 °E,  
133 27.49 °N, 2,990 m a.m.s.l.) is located within the Yadong Valley in the central  
134 Himalayas, while Ali (79.70 °E, 33.39 °N, 4,270 m a.m.s.l.) lies in the western Tibet  
135 at the intersection of the Himalayas, Karakoram, and Gangdise mountain ranges, with  
136 an elevation difference of 1,280 m between these two sites (Fig. 1a). During the  
137 monsoon season, Yadong is primarily influenced by the southwest monsoon and  
138 receives an average annual precipitation of 764.8 mm. In contrast, Fig. 1 shows that  
139 Ali is mainly influenced by the westerlies and has much lower annual precipitation of  
140 105.6 mm, ~70% of which falls during the monsoon season. Temperature at both sites



141 follow a similar seasonal cycle, increasing in spring and summer and decreasing in  
142 autumn and winter. However, due to its higher elevation, Ali is consistently colder  
143 than Yadong, with an annual mean temperature of 2.1 °C compared to 7.2 °C at  
144 Yadong (Fig. 1b).

145 Meteorological data used in this study include surface temperature, precipitation,  
146 relative humidity, and wind speed, recorded at the beginning and end of each  
147 precipitation event. Surface temperature, relative humidity, and wind speed were  
148 averaged between the two measurements, while precipitation was calculated as the  
149 total rainfall amount for each event. Meteorological data for Ali were obtained from a  
150 Campbell ClimaVUE50 automatic weather station installed at the site (with  
151 minute-level temporal resolution), whereas data for Yadong were provided with  
152 hourly resolution. The observation period spans from May 2021 to September 2023 at  
153 both sites.

154 To investigate the influence of ENSO events on precipitation stable isotopes at  
155 Yadong and Ali, we used the monthly Oceanic Niño Index (ONI) provided by the  
156 National Oceanic and Atmospheric Administration Climate Prediction Center (NOAA  
157 CPC,  
158 [https://origin.cpc.ncep.noaa.gov/products/analysis\\_monitoring/ensostuff/ONI\\_v5.php](https://origin.cpc.ncep.noaa.gov/products/analysis_monitoring/ensostuff/ONI_v5.php),  
159 last access: 3 May 2025), based on sea surface temperature (SST) anomalies in the  
160 Niño 3.4 region (5° N-5° S, 120°-170° W).

161

## 162 **2.2 Sample Collection and Measurement**

163 In total, 359 precipitation samples from Yadong and 80 samples from Ali were  
164 analyzed, all collected between May 2021 and September 2023. After each  
165 precipitation event, samples were immediately transferred into 4 ml glass bottles,  
166 sealed, and labeled with event-specific metadata including temperature, precipitation  
167 amount, relative humidity, and wind speed at both the beginning and end of the event.  
168 All samples were stored under refrigeration until isotope measurements.  
169 Measurements of  $\delta^{18}\text{O}$  and  $\delta\text{D}$  were conducted at the State Key Laboratory of Tibetan



170 Plateau Earth System, Environment and Resources, Institute of Tibetan Plateau  
171 Research, Chinese Academy of Sciences (CAS), using a cavity ring-down  
172 spectrometer (Picarro-2130i Liquid Water Isotope Analyzer) with an analytical  
173 precision of  $\pm 0.08$  ‰ for  $\delta^{18}\text{O}$  and  $\pm 0.5$  ‰ for  $\delta\text{D}$ . Isotope values are reported in  
174 delta-notation ( $\delta$ ) relative to Vienna Standard Mean Ocean Water (V-SMOW)  
175 (Dansgaard, 1964):

$$\delta^{18}\text{O} = \left( \frac{\left( \frac{^{18}\text{O}}{^{16}\text{O}} \right)_{\text{sample}}}{\left( \frac{^{18}\text{O}}{^{16}\text{O}} \right)_{\text{standard}}} - 1 \right) \times 1000\text{‰} \quad (1)$$

176 The daily, monthly, seasonal, and annual averages of  $\delta^{18}\text{O}$  are calculated as  
177 precipitation amount-weighted averages:

$$\delta^{18}\text{O}_w = \frac{\sum P_i \delta^{18}\text{O}_i}{\sum P_i} \quad (2)$$

178 where  $P_i$  represents the precipitation amount during the  $i$ -th rainfall event.  $\delta^{18}\text{O}_w$   
179 denotes the precipitation amount-weighted daily, monthly, seasonal, or annual  
180 average.

181

### 182 2.3 Rayleigh Distillation and Mixing Model

183 The Rayleigh distillation model describes the progressive depletion of heavy  
184 isotopes in an air mass as it cools along its trajectory. During this process,  
185 condensation and precipitation preferentially remove the heavier isotopes, leaving the  
186 residual vapor increasingly depleted (Gat, 1996):

$$R = R_0 f^{\alpha_v^l(T)-1} \quad (3)$$

187 where  $R$  and  $R_0$  represent the isotopic ratios of residual and initial vapor,  
188 respectively.  $\alpha_v^l(T)$  denotes the equilibrium fractionation factor, and  $f$  is the fraction  
189 of residual water vapor.

190 By integrating Eq. (1), the Rayleigh distillation model can be expressed as  
191 follows:



$$\delta = (\delta_0 + 1)f_v^{(\alpha_l(T)-1)} - 1 \quad (4)$$

192 where  $\delta$  and  $\delta_0$  are the isotope ratios against V-SMOW in residual and initial vapor,  
193 respectively.

194 To examine the isotopic characteristics after the mixing of two air masses we  
195 employ the following mixing model (Galewsky and Hurley, 2010):

$$R_{\text{mix}} = \frac{f[\text{HDO}]_1 + (1 - f)[\text{HDO}]_2}{f[\text{H}_2\text{O}]_1 + (1 - f)[\text{H}_2\text{O}]_2} \quad (5)$$

196 where  $R_{\text{mix}}$  represents the isotopic ratio of the mixed air mass, while  $[\text{HDO}]$  and  
197  $[\text{H}_2\text{O}]$  denote isotopic water vapor volume mixing ratios.  $f$  is the mixing fraction.

198

## 199 **2.4 Backward Trajectory Calculation and Integrated Water Vapor Flux**

200 To assess the influence of moisture sources on precipitation stable isotopes, we  
201 employed the HYbrid Single-Particle Lagrangian Integrated Trajectory (HYSPLIT)  
202 model developed by the US National Oceanic and Atmospheric Administration  
203 (NOAA) to calculate 120 h backward trajectories for air masses arriving 200 m above  
204 ground level at Yadong and Ali stations. Trajectories were initiated four times daily  
205 (00:00, 06:00, 12:00, and 18:00 UTC) on rainy days between May 2021 and  
206 September 2023. Specific humidity ( $q$ ) variations along each trajectory were also  
207 analyzed. Additionally, HYSPLIT cluster analysis was applied to categorize dominant  
208 transport pathways. The model uses Global Data Assimilation System (GDAS)  
209 reanalysis data with a spatial resolution of  $1^\circ \times 1^\circ$  and a temporal resolution of 6 h,  
210 provided by the National Centers for Environmental Prediction (NCEP,  
211 <ftp://arlftp.arlhq.noaa.gov/archives/gdas1/>, last access: 8 January 2025).

212 We also used ERA5 reanalysis data to calculate integrated water vapor flux from  
213 500 hPa to 200 hPa above the Yadong and Ali sites on rainy days during the study  
214 period. ERA5 data, provided by the European Centre for Medium-Range Weather  
215 Forecasts (ECMWF, <https://cds.climate.copernicus.eu/eu/>, last access: 4 February  
216 2025), include specific humidity ( $q$ ), zonal wind ( $u$ ), and meridional wind ( $v$ )  
217 components, and have a spatial resolution of  $0.25^\circ \times 0.25^\circ$  and temporal resolution of  
218 1 h. These data were used to calculate the integrated water vapor flux ( $Q$ ) using:





$$Q = \frac{1}{g} \int_{P_t}^{P_s} (u, v) q dp \quad (6)$$

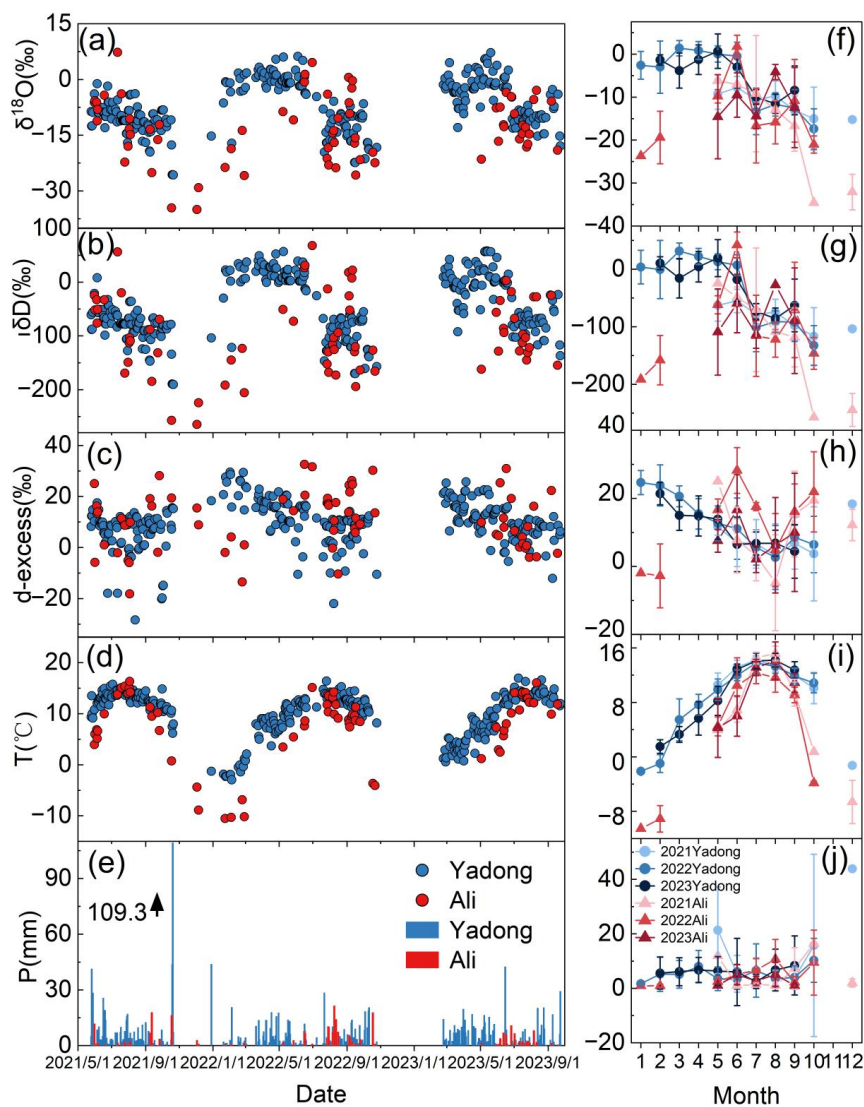
219 where  $g$  is gravitational acceleration, while  $P_s$  and  $P_t$  are surface pressure and top

220 pressure, respectively.

221

## 222 **3 Results**

### 223 **3.1 Temporal Variability of Precipitation Stable Isotopes**



224

225 **Figure 2. Temporal variations of daily precipitation stable isotopes and local**  
 226 **meteorological conditions at Yadong and Ali from May 2021 to September 2023.**  
 227 **(a) and (f) Daily and monthly variations in  $\delta^{18}\text{O}$ . (b) and (g) same as (a) and (f),**  
 228 **but for  $\delta\text{D}$ . (c) and (h) same as (a) and (f), but for d-excess. (d) and (i) same as (a)**  
 229 **and (f), but for temperature. (e) and (j) same as (a) and (f), but for precipitation**  
 230 **amount.**



231

232 To address the influence of the ISM and the westerlies on precipitation stable  
233 isotopes, the year is divided into the monsoon season (June to September) and the  
234 non-monsoon season (October to May of the following year). The non-monsoon  
235 season is further subdivided into the pre-monsoon (March to May), late monsoon  
236 (October), and the westerlies season (November to February).

237 Both Yadong and Ali exhibit remarkable seasonal variations in temperature and  
238 precipitation. Temperatures at both sites follow a unimodal pattern (Fig. 2d and 2i),  
239 peaking in July during the monsoon season at 14.1 °C (Yadong) and 13.3 °C (Ali),  
240 respectively, and reaching their lowest values in January during the non-monsoon  
241 season at −2.1 °C (Yadong) and −10.5 °C (Ali). Also seasonal precipitation patterns  
242 differ significantly between the two sites (Fig. 2e and 2j), with Yadong receiving  
243 substantially higher annual precipitation than Ali (764.8 mm vs. 105.6 mm).  
244 Precipitation at Ali exhibits a strong peak located within the monsoon season (August),  
245 accounting for 70 % of its annual total. In contrast, the precipitation pattern at Yadong  
246 is bimodal, with two peaks in April (pre-monsoon, 118.2 mm, 15.5 % of annual total)  
247 and October (late monsoon, 127.8 mm, 16.7 % of annual total).

248 Both Yadong and Ali exhibit a distinct three-stage isotopic cycle in response to  
249 monsoon evolution:  $\delta^{18}\text{O}$  and  $\delta\text{D}$  increase during the pre-monsoon, moderately  
250 deplete during monsoon development, and reach their lowest values during the late  
251 monsoon season (Fig. 2a–b, Table S1). For instance,  $\delta^{18}\text{O}$  at Yadong decreases from  
252 −2.7 ‰ during the pre-monsoon to −10.7 ‰ during the mature monsoon, reaching  
253 −22.9 ‰ at the end of the monsoon, before rising to −9.6 ‰ under westerly influence.  
254 Ali follows a similar temporal variation, but with more pronounced extremes (from  
255 −8.4 ‰ to −26.7 ‰).

256 Both sites exhibit similar seasonal d-excess pattern (Fig. 2c, Table S1). At Yadong,  
257 d-excess is elevated during the pre-monsoon (15.3 ‰), lowest during the peak  
258 monsoon (6.7 ‰), and then increases again during the late monsoon and westerly  
259 periods (13.1 ‰ and 19.9 ‰, respectively). Similarly, Ali shows high d-excess during



the pre-monsoon (20.9 ‰), a decline during the monsoon (14.0 ‰), a peak in the late monsoon (24.7 ‰), whereas the lowest values during the westerlies (−1.5 ‰) may be attributed to sporadic precipitation events. These variations reflect shifts in moisture sources and the humidity dependence of kinetic fractionation—higher d-excess values are associated with low-humidity sources such as continental or recycled vapor, whereas lower d-excess values correspond to humid or oceanic air masses (Merlivat and Jouzel, 1979; Gat and Matsui, 1991). Ali shows greater amplitude in d-excess changes, especially under westerly influence, indicating a higher sensitivity to shifts between continental and maritime moisture regimes.

Interannual anomalies further highlight the influence of moisture origin and thermal regimes (Fig. 2f, 2h). At Yadong, pre-monsoon (May–June)  $\delta^{18}\text{O}$  was more depleted in 2021 (−9.3 ‰ and −7.8 ‰) but shifted to more enriched values in 2022 (0.0 ‰ and −0.5 ‰) and 2023 (0.7 ‰ and −3.1 ‰), despite only minor changes in d-excess. This indicates enhanced local recycling or warmer vapor source conditions in the latter years. At Ali,  $\delta^{18}\text{O}$  peaked in June 2022 at 1.7 ‰ (compared to −7.1 ‰ in 2021 and −9.5 ‰ in 2023), while in October 2021,  $\delta^{18}\text{O}$  dropped to −34.6 ‰ (vs. −21.0 ‰ in 2022). These fluctuations correspond to d-excess maxima in mid-summer 2022 (28.2 ‰ and 17.6 ‰) and a minimum in August 2021 (−4.8 ‰). These episodic enrichments and depletions are probably resulted from variations in influence of large-scale mode (ENSO), which modulates the humid ISM and the drier westerly regimes, aligning with documented shifts in moisture transport over the TP (Yao et al., 2012).

### 3.2 The Local Meteoric Water Line

**Table 1. Local Meteoric Water Line (LMWL) for Yadong and Ali, including coefficient of determination (R) and p-value.**

Station	Yadong	Ali
Full year	$\delta\text{D} = 8.31 \times \delta^{18}\text{O} + 11.83,$ $R = 0.99, p < 0.01$	$\delta\text{D} = 8.25 \times \delta^{18}\text{O} + 13.76,$ $R = 0.99, p < 0.01$



Pre-monsoon	$\delta D = 7.97 \times \delta^{18}O + 14.64,$ $R = 0.99, p < 0.01$	$\delta D = 8.52 \times \delta^{18}O + 20.38,$ $R = 0.99, p < 0.01$
Monsoon	$\delta D = 7.71 \times \delta^{18}O + 3.58,$ $R = 0.98, p < 0.01$	$\delta D = 8.41 \times \delta^{18}O + 15.07,$ $R = 0.99, p < 0.01$
Late monsoon	$\delta D = 6.77 \times \delta^{18}O - 14.82,$ $R = 0.98, p < 0.01$	$\delta D = 8.37 \times \delta^{18}O + 30.41,$ $R = 0.99, p < 0.01$
Westerlies	$\delta D = 8.34 \times \delta^{18}O + 24.13,$ $R = 0.99, p < 0.01$	$\delta D = 6.84 \times \delta^{18}O - 25.83,$ $R = 0.99, p < 0.01$

286

287 As shown in Fig. S1 and Table 1, the annual LMWL slope and intercept at Yadong  
288 (8.31 and 11.83, respectively) are higher than those of the GMWL (8 and 10), which  
289 may reflect strong vapor recycling. During the pre-monsoon, the slope (7.97)  
290 approximates that of the GMWL, while the intercept is higher (14.64), suggesting a  
291 moisture source with relatively low humidity compared to the monsoon and late  
292 monsoon seasons. During the monsoon and late monsoon, both the slopes (7.71 and  
293 6.77) and intercepts (3.58 and -14.82) fall below the GMWL, indicating influence  
294 from sub-cloud evaporation and humid moisture sources. In contrast, the LMWL  
295 slope and intercept during the westerlies season (8.34 and 24.13) exceed those of the  
296 GMWL, likely due to enhanced moisture recycling. These findings are consistent with  
297 previous reports, such as an annual LMWL slope and intercept of 8.4 and 12.02 at  
298 Yadong (Axelsson et al., 2023). Notably, the LMWL at Yadong during the monsoon  
299 closely resembles that of Naqu (slope = 7.67, intercept = 1.3) in the central TP (Li et  
300 al., 2023).

301 At Ali, the LMWL slopes (8.25, 8.52, 8.41, and 8.37) and intercepts (13.76, 20.38,  
302 15.07, and 30.41) are consistently higher than the GMWL during the annual,  
303 pre-monsoon, monsoon, and late monsoon seasons, suggesting dominance of moisture  
304 recycling. However, during the westerlies season, the slope (6.84) and intercept  
305 (-25.83) are substantially lower, indicating strong sub-cloud evaporation and humid  
306 moisture sources. This may result from synoptic transport from oceanic sources,



307 which is discussed in detail in section 3.4.

308

### 309 **3.3 The Influence of Local Meteorological Factors**

310 At Yadong,  $\delta^{18}\text{O}$  exhibits a significant negative correlation with temperature  
311 throughout the year (slope =  $-0.27$ ,  $R = -0.42$ ,  $p < 0.001$ ). Seasonally, this  
312 relationship is negative from the late pre-monsoon to late monsoon ( $R = -0.30$ ,  $p <$   
313  $0.001$ ), but shifts to a significant positive correlation from the westerlies to the early  
314 pre-monsoon of the following year ( $R = 0.51$ ,  $p < 0.001$ ), indicating a clear seasonal  
315 reversal in the temperature effect. At Ali,  $\delta^{18}\text{O}$  is positively correlated with  
316 temperature year-round (slope =  $0.30$ ,  $R = 0.39$ ,  $p < 0.001$ ), with the strongest  
317 correlation observed from the late monsoon to the pre-monsoon season of the  
318 following year ( $R = 0.79$ ,  $p < 0.001$ ).

319 In terms of precipitation,  $\delta^{18}\text{O}$  at Yadong is significantly negatively correlated  
320 year-round (slope =  $-0.35$ ,  $R = -0.25$ ,  $p < 0.001$ ), and particularly from the late  
321 pre-monsoon to late monsoon ( $R = -0.28$ ,  $p < 0.001$ ), reflecting a typical amount  
322 effect. This correlation intensifies during the westerlies to early pre-monsoon season  
323 ( $R = -0.49$ ,  $p < 0.001$ ). At Ali, a significant negative correlation between  $\delta^{18}\text{O}$  and  
324 precipitation is only observed during the monsoon season ( $R = -0.32$ ,  $p < 0.05$ ),  
325 associated with the missing of temperature effect.

326 Regarding wind speed,  $\delta^{18}\text{O}$  at Yadong shows a weak negative correlation over the  
327 full year (slope =  $-0.02$ ,  $R = -0.11$ ,  $p < 0.05$ ), whereas at Ali, it is significantly  
328 positively correlated year-round (slope =  $0.04$ ,  $R = 0.34$ ,  $p < 0.01$ ), with the strongest  
329 relationship during the late monsoon to pre-monsoon ( $R = 0.66$ ,  $p < 0.001$ ), associated  
330 with the strongest temperature effect (Fig. S2).

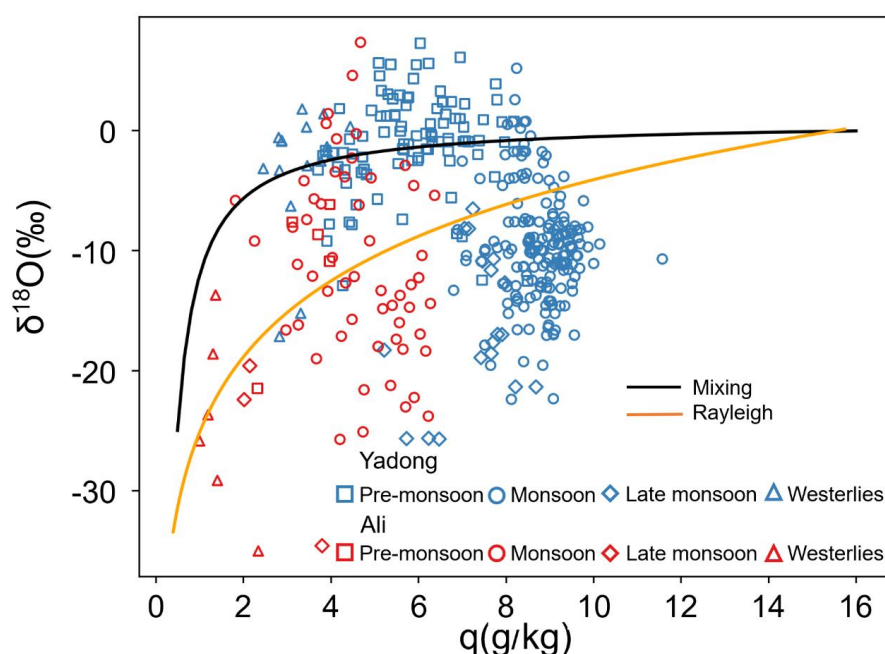
331 These results indicate that Yadong is predominantly influenced by the monsoon  
332 from the late pre-monsoon to late monsoon season, characterized by a strong amount  
333 effect. From the westerlies to early pre-monsoon, it is mainly affected by westerly  
334 winds and local moisture recycling, exhibiting a significant temperature effect. In  
335 contrast, Ali is primarily influenced by the monsoon during the monsoon season,



336 showing a clear amount effect, and by westerlies and local vapor recycling from the  
337 late monsoon to pre-monsoon, where the temperature effect becomes significant.  
338 These observations are consistent with previous studies reporting a significant amount  
339 effect in the southern TP, including at Bomi and Lhasa (Gao et al., 2011), and a  
340 dominant temperature effect in the northwestern TP, such as in the Bagrot Valley  
341 (Wang et al., 2019).

342

### 343 3.4 The Influence of Moisture Transport Processes



344

345 **Figure 3. Scatter plot of  $\delta^{18}\text{O}$  versus specific humidity ( $q$ ) at Yadong and Ali.**  
346 **Black and orange lines represent the mixing and Rayleigh fractionation curves,**  
347 **respectively. The Rayleigh starting point is set at  $-0.07\text{‰}$  and  $16\text{ g kg}^{-1}$  at  $25\text{ °C}$ ,**  
348 **assuming equilibrium conditions for precipitation from sea-level air with  $80\%$**   
349 **relative humidity. The mixing curve uses the same wet end-member; the dry**  
350 **end-member is set at  $-25\text{‰}$  and  $0.5\text{ g kg}^{-1}$ .**

351

352 The  $q$ - $\delta^{18}\text{O}$  relationship effectively reflects seasonal controls on precipitation



353 isotopes at both sites (Fig. 3). At Yadong, during the pre-monsoon and westerlies  
354 seasons, most  $\delta^{18}\text{O}$  values lie above the mixing curve, indicating substantial influence  
355 from local surface evaporation. In contrast, during the monsoon and late monsoon,  
356 most  $\delta^{18}\text{O}$  values fall below the Rayleigh curve, suggesting dominant effects of  
357 sub-cloud evaporation and rainout effect, consistent with prior LMWL-based  
358 interpretations. Some monsoon-season values fall between the Rayleigh and mixing  
359 curves, reflecting contributions from moisture mixing process.

360 At Ali,  $\delta^{18}\text{O}$  values during the pre-monsoon, monsoon, and westerlies seasons fall  
361 between the Rayleigh and mixing curves, indicating joint control by moisture mixing  
362 and precipitation processes. Notably, during the monsoon, late monsoon, and  
363 westerlies seasons, many  $\delta^{18}\text{O}$  values fall below the Rayleigh curve, suggesting  
364 sub-cloud evaporation is also influential, consistent with Ali's LMWL during these  
365 seasons.

366 The isotope–humidity contrast between the two sites is clearest during the  
367 westerlies season:  $\delta^{18}\text{O}$  averages  $-9.6\text{‰}$  at Yadong and  $-21.8\text{‰}$  at Ali, with  
368 corresponding  $q$  values of  $3.3\text{ g kg}^{-1}$  and  $1.4\text{ g kg}^{-1}$ . In contrast, during the monsoon  
369 season,  $\delta^{18}\text{O}$  averages converge ( $-10.7\text{‰}$  at Yadong vs.  $-13.3\text{‰}$  at Ali) with  
370 consistent magnitudes, but  $q$  is nearly double at Yadong ( $8.8\text{ g kg}^{-1}$  vs.  $4.7\text{ g kg}^{-1}$ ).

371 In summary, monsoon-season  $\delta^{18}\text{O}$  at both sites reflects combined influences of  
372 sub-cloud evaporation, mixing, and rainout effect. Under westerly conditions,  $\delta^{18}\text{O}$  at  
373 Yadong is more influenced by local evaporation, while  $\delta^{18}\text{O}$  at Ali is influenced by  
374 Rayleigh-type fractionation and moisture mixing, leading to consistently lower  $\delta^{18}\text{O}$   
375 values.



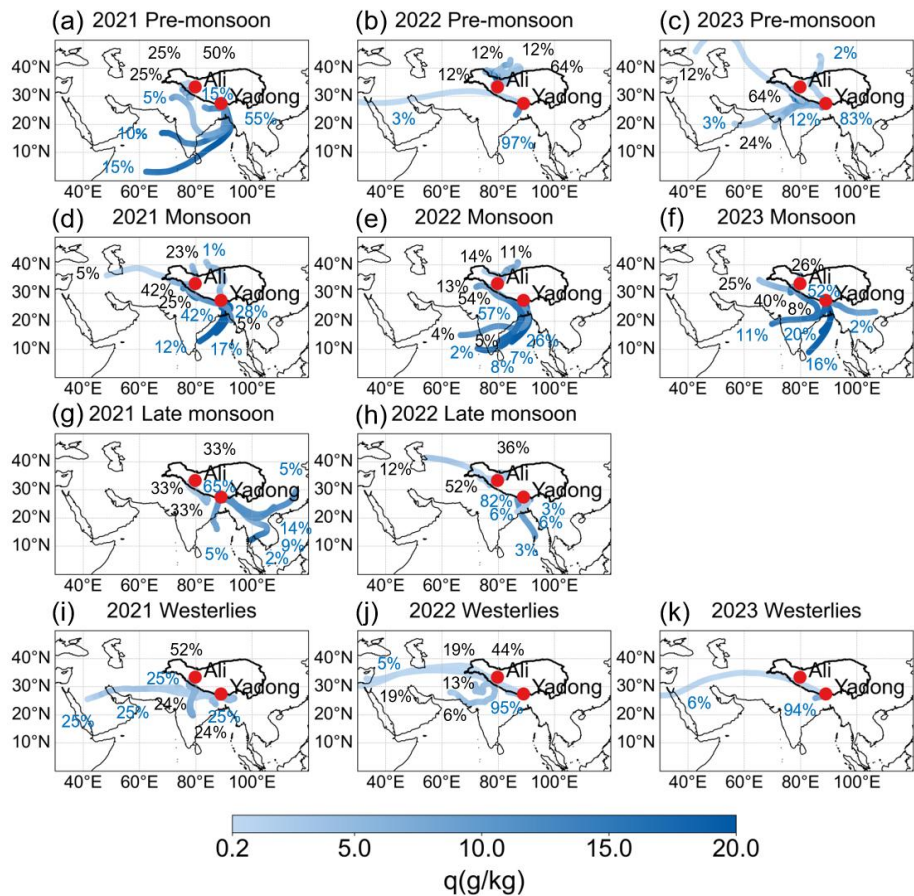


**Figure 4. Clustered backward trajectories for Yadong and Ali during the pre-monsoon, monsoon, late monsoon, and westerlies seasons. Red dots show the locations of both sites. Trajectory colors indicate changes in  $q$ , while numbers indicate the proportion of clustered trajectories to total trajectories at Yadong and Ali.**

$\delta^{18}\text{O}$  and d-excess in precipitation at Yadong and Ali during our observation periods reveal consistent distribution ranges and diurnal variability during the monsoon season, implying consistent moisture origins. To delineate seasonal and interannual insight into moisture sources and transport pathways variability, we employed the HYSPLIT model to compute 120 h backward trajectories for rainy days,



388 covering four climatological intervals: pre-monsoon, mature monsoon, late monsoon,  
389 and westerly-dominated seasons. During May (pre-monsoon) 2021, Yadong received  
390 high-humidity ISM moisture, with contribution from the BOB (55 %) and AS (25 %) (Fig. 4a),  
391 resulting in a relatively depleted  $\delta^{18}\text{O}$  average of  $-9.3\text{‰}$ . In contrast, in  
392 May 2022-2023, local surface evapotranspiration (97 % and 83 %, respectively)  
393 combined with low - humidity westerly (both are 3 %) produced a bit enriched  $\delta^{18}\text{O}$   
394 average (Fig. 4b-c). During the mature monsoon season, in 2021-2022 (Fig. 4d-e),  
395 high-humidity ISM (57 % and 43 %, respectively) combined with local surface  
396 evapotranspiration (42 % and 57 %, respectively) consistently supplied moisture to  
397 Yadong, while in 2023 (Fig. 4f), moisture mainly contributed from the BOB (36 %) and  
398 moist Indian subcontinent as well as local recycling (63 %) resulted in  $\delta^{18}\text{O}$   
399 average of  $-10.7\text{‰}$  and d-excess of  $6.7\text{‰}$ . During the late monsoon season (Fig. 4g-h),  
400 the contribution from ISM (7 % in 2021 and 18 % in 2022) and East Asian monsoon (28 % in 2021)  
401 resulted in depleted  $\delta^{18}\text{O}$  to  $-22.9\text{‰}$  and raised d-excess to  $13.1\text{‰}$ . During the westerlies season (Fig. 4i-k),  
402 the higher contribution from low-humidity westerly (75 %) in 2021 resulted in depleted  $\delta^{18}\text{O}$  to  $-15.2\text{‰}$  and  
403 d-excess to  $18.3\text{‰}$ , compared to those in 2022 and 2023.

405 Ali exhibited distinct seasonal patterns. During the pre-monsoon season, in  
406 2021-2022 (Fig. 4a-b), moisture mainly contributed from local recycling, while in  
407 2023 (Fig. 4c), Ali received additional moisture from the low-humidity westerly (12 %) and AS (24 %),  
408 resulting in  $\delta^{18}\text{O}$  average of  $-8.4\text{‰}$  and d-excess of  $20.9\text{‰}$ . During the monsoon, in 2021-2022 (Fig. 4d-e),  
409 high-humidity ISM (5 % and 9 %, respectively) combined with local surface evapotranspiration and  
410 moist Indian subcontinent (67 % and 54 %, respectively) consistently supplied moisture to Ali,  
411 while in 2023 (Fig. 4f), moisture mainly contributed from the eastern Indian subcontinent and local  
412 circulation (74 %), resulting in  $\delta^{18}\text{O}$  averaged of  $-13.3\text{‰}$  and d-excess of  $14.0\text{‰}$ . In October 2021 (Fig. 4g),  
413 Ali was influenced by dry northeastern Indian sources, producing extremely depleted  $\delta^{18}\text{O}$  of  $-34.6\text{‰}$ ,  
414 compare to  $-21.0\text{‰}$  in October 2022 (Fig. 4h), when moisture mainly contributed from westerlies (12 %)



417 and western Tibet (88 %). During the westerlies season (Fig. 4i-j), Ali received both  
418 high-humidity moisture from Indian sources and dry long-range continental moisture  
419 via westerly winds, yielding a markedly depleted average  $\delta^{18}\text{O}$  of  $-21.8\text{ ‰}$  and  
420 moderate d-excess of  $-1.5\text{ ‰}$ .

421 Thus, monsoon-season convergence of  $\delta^{18}\text{O}$  values ( $-10.7\text{ ‰}$  at Yadong,  $-13.3\text{ ‰}$   
422 at Ali) reflects a shared ISM moisture source, whereas the westerlies-season  
423 divergence of  $\delta^{18}\text{O}$  is largest ( $-9.6\text{ ‰}$  at Yadong,  $-21.8\text{ ‰}$  at Ali) due to differing  
424 moisture regimes.

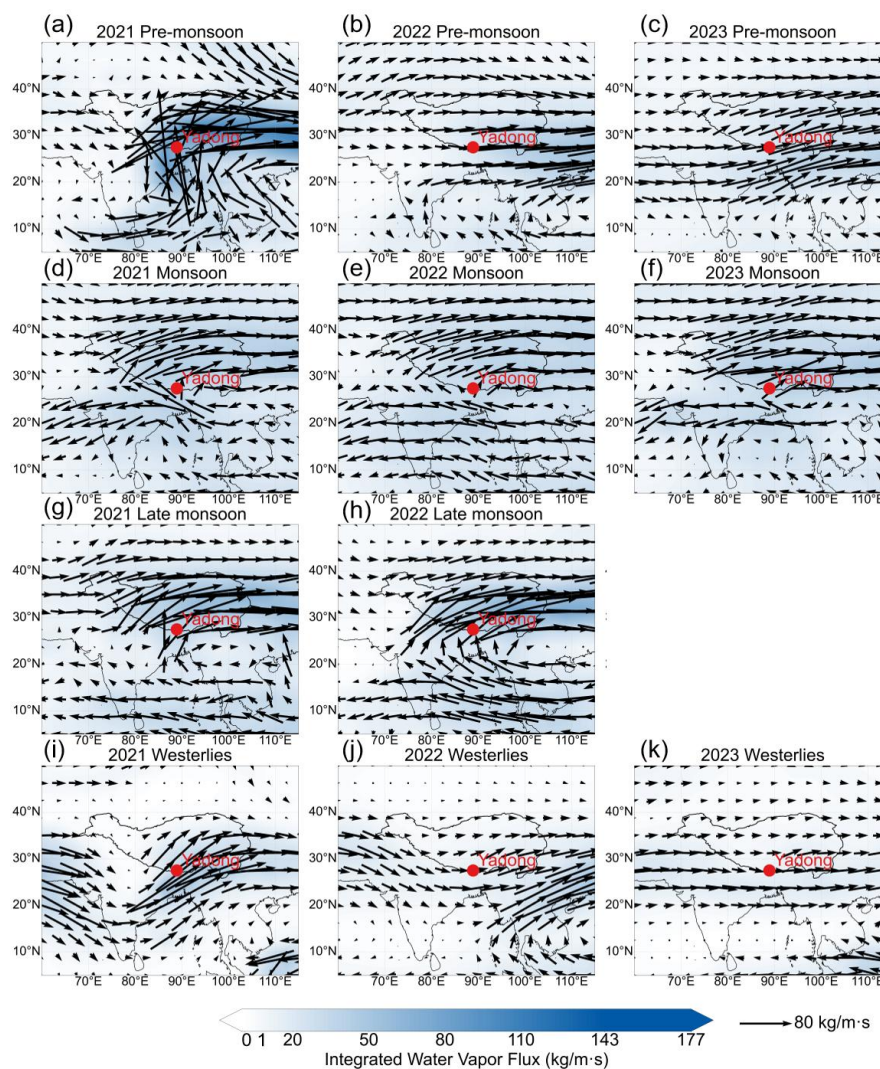


**Figure 5. Integrated water vapor flux (500-200 hPa) over Yadong across seasons (the length and direction of the black arrows indicate the magnitude and direction of water vapor flux).**



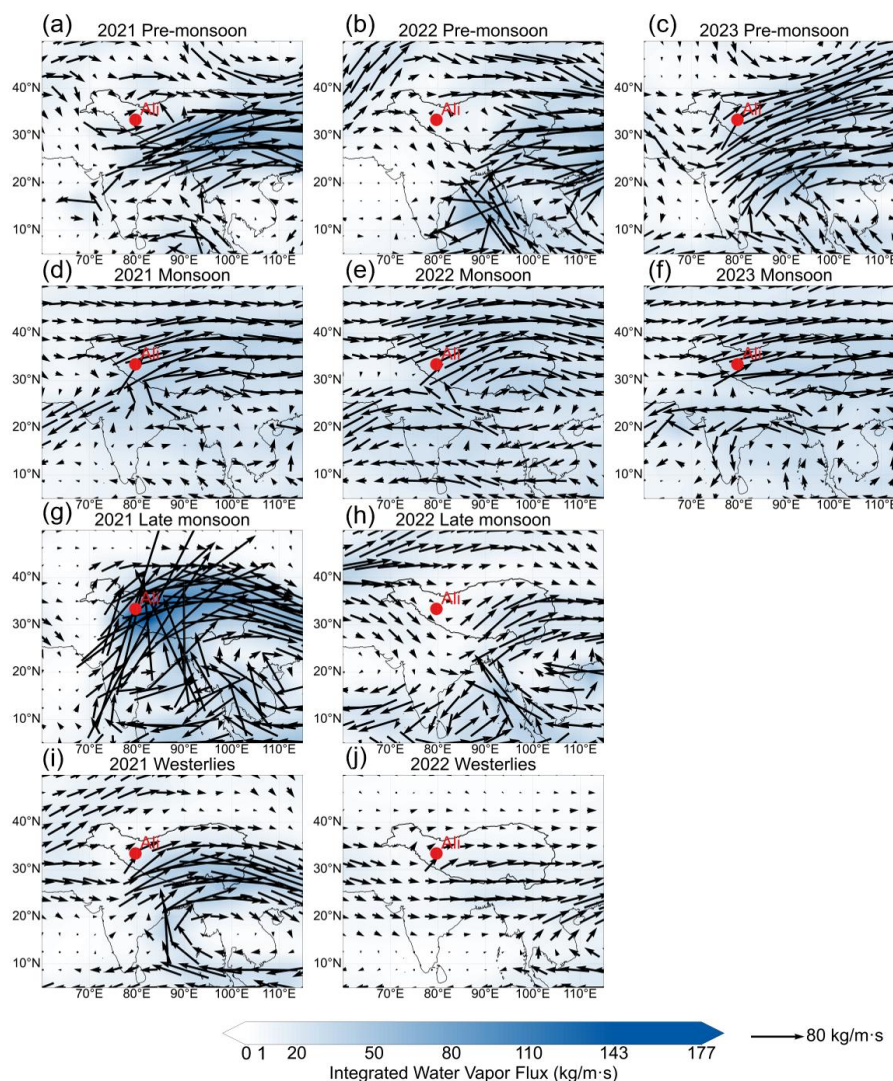


**Figure 6 Integrated water vapor flux (500-200 hPa) over Ali across seasons (the length and direction of the black arrows indicate the magnitude and direction of water vapor flux).**

At Yadong, ISM dominated the moisture transport during pre-monsoon of 2021, with maximum water vapor flux reaching  $77.5 \text{ kg m}^{-1} \text{ s}^{-1}$  (Fig. 5a), yielding lower  $\delta^{18}\text{O}$  of  $-9.3 \text{ ‰}$ . In 2022 and 2023, Yadong was controlled by dry westerly, resulting in a reduction in water vapor flux to  $24.6 \text{ kg m}^{-1} \text{ s}^{-1}$  (Fig. 5b) and  $23.3 \text{ kg m}^{-1} \text{ s}^{-1}$  (Fig.



438 5c), respectively, and corresponding increase in the average  $\delta^{18}\text{O}$  values of 9.3 ‰ and  
439 10.0 ‰ compared to 2021. During the monsoon season, the dominant circulation  
440 shifted from westerlies to monsoon, with water vapor flux increasing to  $32.5 \text{ kg m}^{-1}$   
441  $\text{s}^{-1}$ , and the average  $\delta^{18}\text{O}$  value decreasing by  $\sim 8.0$  ‰ relative to the pre-monsoon  
442 season (Fig. 5d-f). In the late monsoon season, water vapor flux reached a seasonal  
443 high of  $39.6 \text{ kg m}^{-1} \text{ s}^{-1}$  (Fig. 5g-h), while the average  $\delta^{18}\text{O}$  decreased by an additional  
444 12.2 ‰. During the westerlies season, westerly carried dryer moisture to this region,  
445 resulting in a reduction in water vapor flux to  $22.2 \text{ kg m}^{-1} \text{ s}^{-1}$  (Fig. 5i-k), and a  
446 13.3 ‰ increase in average  $\delta^{18}\text{O}$  values compared to the late monsoon.

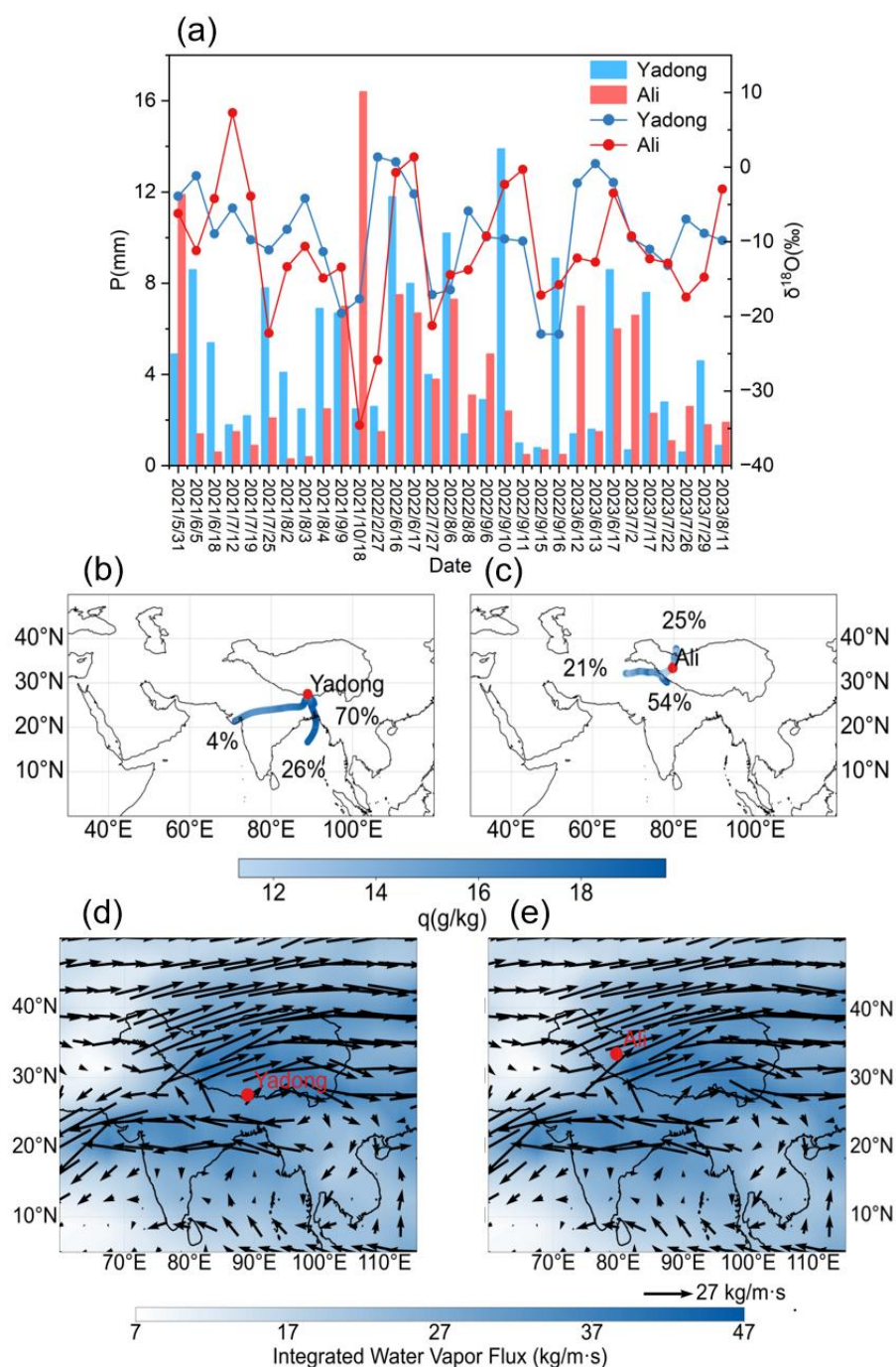
447 During the pre-monsoon period (Fig. 6a-c), Ali was dominated by the westerly,  
448 with a relatively low water vapor flux of  $18.6 \text{ kg m}^{-1} \text{ s}^{-1}$  and an average  $\delta^{18}\text{O}$  value of  
449  $-8.4$  ‰. During the monsoon season (Fig. 6d-f), the region transitions to monsoon  
450 dominance, resulting in an increase in water vapor flux to  $36.5 \text{ kg m}^{-1} \text{ s}^{-1}$  and a  
451 corresponding decrease in the average  $\delta^{18}\text{O}$  by 4.9 ‰. During the late monsoon  
452 season, substantial interannual variability was observed. In 2021 (Fig. 6g), the region  
453 remained under the monsoon influence, with the maximum water vapor flux reaching  
454  $98.6 \text{ kg m}^{-1} \text{ s}^{-1}$ . In contrast, the region shifted to westerly dominance in 2022 (Fig.  
455 6h), leading to a sharp decline in water vapor flux to  $5.5 \text{ kg m}^{-1} \text{ s}^{-1}$ , and an increase in  
456 the average  $\delta^{18}\text{O}$  of 13.6 ‰ compared to 2021. During the westerlies season,  
457 persistent westerly influence resulted in a further decrease in water vapor flux to  $11.5$   
458  $\text{kg m}^{-1} \text{ s}^{-1}$ , accompanied by an increase in average  $\delta^{18}\text{O}$  of 4.9 ‰ relative to the late  
459 monsoon season.

460 These results demonstrate that seasonal and interannual variations in  
461 ISM-westerly patterns exert strong control over both moisture transport and  
462 precipitation isotope compositions at both Yadong and Ali. The systematic inverse  
463 relationship between water vapor flux and  $\delta^{18}\text{O}$  values reflects the fundamental  
464 influence of moisture source regions and transport pathways on isotopic signatures,  
465 with monsoon-sourced moisture consistently producing higher flux and more depleted  
466 isotopic signatures compared to westerly-transported moisture. The pronounced



467 interannual variability observed during the late monsoon season, particularly the  
468 contrasting circulation patterns between 2021 and 2022, highlights the sensitivity of  
469 precipitation stable isotopes to large-scale atmospheric dynamics.

470 **3.5 Moisture Sources on Simultaneous Rainy Days**



471

472 **Figure 7. (a)  $\delta^{18}\text{O}$  and  $P$  on simultaneous rainy days at Yadong and Ali;**

473 **backward trajectories on simultaneous rainy days at Yadong (b) and Ali (c)**





474 **during the monsoon season; integrated water vapor flux from 500 hPa to 200**  
475 **hPa on simultaneous rainy days at Yadong (d) and Ali (e) during the monsoon**  
476 **season.**

477

478 During the monsoon season, simultaneous precipitation events were recorded on  
479 28 days at both Yadong and Ali, whereas only 3 such days were observed during the  
480 non-monsoon season (Fig. 7a). During the monsoon season, the average  $\delta^{18}\text{O}$  values  
481 for simultaneous precipitation days at Yadong and Ali were  $-9.3\text{‰}$  and  $-9.4\text{‰}$ ,  
482 respectively, with corresponding average d-excess values of  $9.2\text{‰}$  and  $13.9\text{‰}$ .  
483 Precipitation amounts at Yadong (137.9 mm) exceeded those at Ali (84.9 mm) by 53  
484 mm, likely resulting from Yadong's more southeastward location and 1280 m lower  
485 altitude under the ISM influence.

486 In contrast, during the non-monsoon season, concurrent precipitation events  
487 exhibited a reversal of the monsoon-season pattern. The average  $\delta^{18}\text{O}$  values on  
488 concurrent precipitation events were  $-6.0\text{‰}$  and  $-22.8\text{‰}$ , respectively, with  
489 d-excess averages of  $10.7\text{‰}$  and  $20.7\text{‰}$ , and precipitation amounts of 10.0 mm and  
490 29.8 mm, respectively. The large differences in  $\delta^{18}\text{O}$  ( $16.8\text{‰}$ ) and d-excess ( $10.0\text{‰}$ )  
491 indicate distinct moisture sources, with Yadong influenced by more local or recycled  
492 moisture and Ali influenced by more continental or long-distance transported westerly  
493 moisture.

494 Backward trajectory analysis supports further these findings. During  
495 monsoon-season simultaneous events, the ISM transports large amounts of  
496 high-humidity moisture to Yadong, along with contributions from local surface  
497 evapotranspiration (Fig. 7b and S3a). In contrast, Ali's moisture primarily originates  
498 from local evapotranspiration (Fig. 7c), supplemented by high-humidity ISM input  
499 and smaller contributions from low-humidity westerly winds (Fig. S3b), indicating  
500 that the ISM simultaneously influences both Yadong and Ali at the synoptic scale.  
501 This conclusion is further supported by water vapor flux analysis (Fig. 7d and 7e),  
502 exhibiting pronounced high flux of  $33.0\text{ kg m}^{-1}\text{ s}^{-1}$  at Yadong and  $36.2\text{ kg m}^{-1}\text{ s}^{-1}$  at



Ali. The strength and coherence of monsoonal moisture transport across both regions highlight the ISM's crucial role in controlling precipitation isotopic signatures during simultaneous events at the southern and western TP.

3.6 The Influence of ENSO events

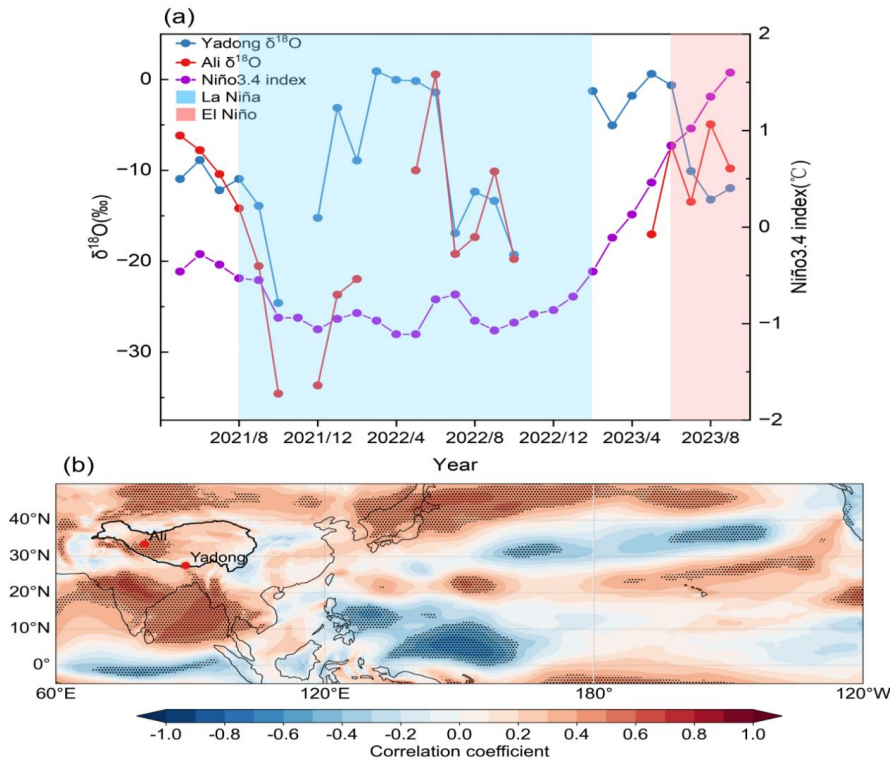


**Figure 8. (a) Time series of the monthly Niño 3.4 index and monthly amount-weighted  $\delta^{18}\text{O}$  values at Yadong and Ali from May 2021 to September 2023. El Niño and La Niña periods are highlighted in red and blue shading, respectively. (b) Spatial correlation between the monthly Niño 3.4 index and monthly mean integrated water vapor flux (surface to 200 hPa) during the same period. The correlation coefficient reveals regions of enhanced or suppressed moisture transport associated with ENSO phases.**

The period from August 2021 to January 2023 was characterized by La Niña



518 conditions, while June to September 2023 coincided with an El Niño phase.  
519 Precipitation  $\delta^{18}\text{O}$  values at Yadong and Ali during the monsoon seasons reflect a  
520 clear ENSO imprint. During the monsoon season in 2021, average  $\delta^{18}\text{O}$  values at  
521 Yadong and Ali were  $-11.2\text{‰}$  and  $-17.2\text{‰}$ , respectively. During the same period in  
522 2022 (La Niña events),  $\delta^{18}\text{O}$  values are consistent with those in 2021, while in 2023  
523 (El Niño),  $\delta^{18}\text{O}$  increased sharply to  $-8.9\text{‰}$  at Yadong and  $-9.1\text{‰}$  at Ali,  
524 respectively. The most pronounced increases in  $\delta^{18}\text{O}$  occurred between the La Niña  
525 and El Niño monsoon seasons indicate that ENSO significantly influences the  
526 interannual variability of precipitation stable isotopes at both sites, which is consistent  
527 with previous studies (Gao et al., 2018) (Fig. 8a).

528 To further explore the underlying mechanisms, spatial correlation analysis was  
529 conducted between the monthly Niño 3.4 index and the monthly mean integrated  
530 water vapor flux (surface to 200 hPa) for May 2021 to September 2023 (Fig. 8b).  
531 Results show that significant positive correlations ( $p < 0.05$ ) existed over Ali, the AS,  
532 Indian subcontinent, BOB, and Bangladesh. In contrast, significant negative  
533 correlations appeared over the equatorial Indian Ocean and western equatorial Pacific,  
534 pointing to major shifts in regional moisture transport pathways during ENSO events.

535 During El Niño events, warm sea surface temperature anomalies (SSTA) develop  
536 in the eastern equatorial Pacific, which reduce the east–west SST gradient. This  
537 weakens the Walker circulation, and results in westerly wind anomalies in the  
538 equatorial Pacific (Bjerknes, 1969). Concurrently, SSTs in the western equatorial  
539 Pacific decrease, leading to suppressed surface evaporation and moisture advection,  
540 along with anomalously weak convection over that region. In contrast, the region  
541 south of the southern TP, including Bangladesh, the BOB, the Indian subcontinent,  
542 and the AS, experience increased temperature, enhanced surface evaporation and  
543 moisture advection, and anomalously convection, accompanied by low-level easterly  
544 wind anomalies (Yao et al., 2024). Together, these anomalies form a zonal–vertical  
545 atmospheric circulation pattern (Wang et al., 2024). Additionally, cooling in the  
546 equatorial Indian Ocean suppresses surface evaporation and moisture flux, and



547 weakens southerly wind anomalies toward the TP. These circulation changes result  
548 in reduced ISM moisture transport to both Yadong (from 43 % in 2022 to 36 % in  
549 2023) and Ali (from 9 % in 2022 to 0 % in 2023), while contributions of local  
550 evapotranspiration and short-distance transport from south moist continental surface  
551 increased relatively (from 57 % in 2022 to 63 % in 2023 at Yadong and from 54 % in  
552 2022 to 74 % in 2023 at Ali) (Fig. 4e-f and 8b). This leads to more enriched  $\delta^{18}\text{O}$   
553 values at Yadong and Ali during El Niño years (Cui et al., 2025).

554 The atmospheric circulation patterns during La Niña events are essentially the  
555 inverse of those during El Niño (Cai and Tian, 2016). La Niña strengthens the Walker  
556 circulation, with elevated SSTs in the western equatorial Pacific leading to enhanced  
557 surface evaporation, increased water vapor flux, and strong anomalous convection. At  
558 the same time, SSTs rise in the equatorial Indian Ocean, enhancing surface  
559 evaporation and northward moisture advection, resulting in increased ISM moisture  
560 transport to both Yadong and Ali. This process contributes to significant  $\delta^{18}\text{O}$   
561 depletion during La Niña events at Yadong and Ali (Fig. 4e-f and 8b).

562

#### 563 **4 Summary and Conclusions**

564 This study characterized event-based precipitation stable isotopes ( $\delta^{18}\text{O}$ ,  $\delta\text{D}$ ) at  
565 Yadong and Ali from May 2021 to September 2023 to investigate climate controls of  
566 variability in precipitation stable isotopes on the TP across daily, synoptic, seasonal,  
567 and interannual scales. We characterize the influence of shifting moisture sources  
568 under westerly and ISM transport regimes, and the differential impact of El Niño and  
569 La Niña events on precipitation isotopes.

570 Our results show that  $\delta^{18}\text{O}$  and  $\delta\text{D}$  at Yadong and Ali converge during the  
571 monsoon season but diverge sharply during the westerlies season, reaching  
572 differences of up to 12.2 ‰ and 118.8 ‰, respectively. While d-excess values remain  
573 similar during the pre-monsoon and monsoon seasons, they diverge significantly in  
574 the late monsoon and westerlies seasons, reaching respective differences of 11.6 ‰  
575 and 21.4 ‰.



576 Our results also show that meteorological controls shift seasonally: 1)  
577 precipitation amount effects dominate during monsoon ( $R = -0.28$  to  $-0.32$ ), while  
578 temperature controls prevail during westerly seasons ( $R = 0.51$ – $0.79$ ); 2) during the  
579 monsoon, both sites reflect moisture mixing, rainout effect, and sub-cloud  
580 evaporation, closely aligned with  $\delta^{18}\text{O}$  changes; however, during the westerlies season,  
581 Yadong is influenced primarily by local evaporation, whereas Ali is shaped by  
582 Rayleigh fractionation and long-range continental transport, resulting in pronounced  
583  $\delta^{18}\text{O}$  differences ( $-9.6\text{‰}$  vs.  $-21.8\text{‰}$ ); 3) atmospheric moisture at both sites are  
584 primarily supplied by the seasonally shifted ISM and westerly, accompanied by local  
585 and mid-latitude dry sources at Yadong and long-distance continental moisture at Ali,  
586 explaining the seasonal convergence and divergence in  $\delta^{18}\text{O}$  patterns; 4)  $\delta^{18}\text{O}$   
587 variations in 28 simultaneous precipitation events during the monsoon season suggest  
588 ISM dominance at both sites during these events.

589 Our results further confirm that interannual variability in precipitation  $\delta^{18}\text{O}$  at both  
590 sites is clearly linked to ENSO, with  $\delta^{18}\text{O}$  enrichment of  $2.8\text{‰}$  (Yadong) and  $5.1\text{‰}$   
591 (Ali) from 2022 La Niña to 2023 El Niño monsoon seasons. This enrichment results  
592 from changes of moisture transport related with ENSO events. During El Niño events,  
593 weakened Walker circulation and reduced ISM moisture transport increase the relative  
594 contributions of local evapotranspiration and short-distance transport from southern  
595 moist continental surfaces, leading to precipitation  $\delta^{18}\text{O}$  enrichment. Conversely, La  
596 Niña events strengthen the Walker circulation and enhance ISM moisture transport  
597 through elevated western Pacific and Indian Ocean SSTs, resulting in significant  
598 precipitation  $\delta^{18}\text{O}$  depletion at both sites.

599 Our results demonstrate that ISM circulation homogenizes isotopic signatures  
600 across the southern and western Tibetan Plateau, while westerly dominance amplifies  
601 regional differences through distinct moisture pathways. The seasonal transition from  
602 amount-controlled to temperature-controlled isotopic variability reflects fundamental  
603 changes in precipitation isotopic mechanisms. The pronounced ENSO sensitivity  
604 indicates that tropical Pacific variability significantly modulates regional hydrological



605 processes through altered moisture transport patterns.

606 Our findings align with previous studies showing ISM dominance in summer  
607 isotopic patterns across the Tibetan Plateau, but provide new quantitative constraints  
608 on seasonal moisture source transitions. The documented ENSO influence on  
609 precipitation isotopes (2.8–5.1 ‰ variability) exceeds previously reported values from  
610 limited observations, highlighting the importance of multi-year datasets for capturing  
611 interannual climate impacts. Our  $\delta$  analysis advances understanding of site-specific  
612 responses to sub-cloud evaporation and moisture recycling that were sparsely resolved  
613 in earlier regional studies.

614 This study provides critical observational constraints for atmospheric moisture  
615 transport and regional climate sensitivity in the Tibetan Plateau. The quantified ENSO  
616 sensitivity of precipitation isotopes offers new insights on regional paleoclimate  
617 records interpretation. The 3-year sampling period, however, limits our ability to  
618 assess decadal-scale variability and multi-ENSO cycle impacts. Future work should  
619 extend observations to capture longer-term climate oscillations and validate these  
620 findings across broader spatial scales. Additionally, the mechanisms driving the  
621 observed local evapotranspiration changes during ENSO events require further  
622 investigation through integrated land-atmosphere modeling approaches.

623

#### 624 **Data availability:**

625 The ERA5 dataset is the latest reanalysis dataset published by the European  
626 Centre for Medium-Range Weather Forecasts (ECMWF) available at  
627 <https://doi.org/10.24381/cds.bd0915c6> (Hersbach et al., 2023). The Global Data  
628 Assimilation System (GDAS) has been published by the National Centers for  
629 Environmental Prediction (NCEP) (<ftp://arlftp.arlhq.noaa.gov/archives/gdas1/>, NCEP,  
630 2024). The monthly Oceanic Niño Index (ONI) provided by the National Oceanic and  
631 Atmospheric Administration Climate Prediction Center (NOAA CPC)  
632 ([https://origin.cpc.ncep.noaa.gov/products/analysis\\_monitoring/ensostuff/ONI\\_v5.php](https://origin.cpc.ncep.noaa.gov/products/analysis_monitoring/ensostuff/ONI_v5.php))  
633 . The precipitation isotopic compositions dataset will be available on the Zenodo



634 research data repository after manuscript publication.

635

636 **Author contributions:**

637 **LK:** data curation, formal analysis, writing (original draft preparation). **GJ:** data  
638 curation, conceptualization, methodology, supervision, writing (review and editing),  
639 funding acquisition. **YJJ:** data curation. **NXW:** data curation. **ZAB:** writing (review  
640 and editing), project administration. **CGBR:** data curation. **WYQ:** data curation.  
641 **LYG:** data curation.

642

643 **Competing interests:**

644 The contact author has declared that none of the authors has any competing interests.

645

646 **Acknowledgements:**

647 This work was funded by The Second Tibetan Plateau Scientific Expedition and  
648 Research (STEP) program (grant no. 2024QZKK0400) and the National Natural  
649 Science Foundation of China (grant nos. 41922002), as well as the Innovation  
650 Program for Young Scholars of TPESER (QNCX2022ZD-01). We acknowledge the  
651 staff at the two observational stations for collecting the precipitation samples. We  
652 extend our sincere thanks to Sonja Wahl and Laura Jasmin Dietrich for their fruitful  
653 suggestions.

654

655 **Financial support:**

656 This research has been supported by the Second Tibetan Plateau Scientific  
657 Expedition and Research (STEP) program (grant no. 2024QZKK0400) and the  
658 National Natural Science Foundation of China (grant no. 41922002), as well as the  
659 Innovation Program for Young Scholars of TPESER (QNCX2022ZD-01).

660

661 **References**

662 Adhikari, N., Gao, J., Yao, T., Yang, Y., and Dai, D.: The main controls of the



- 663 precipitation stable isotopes at Kathmandu, Nepal, *Tellus B: Chemical and*  
664 *Physical Meteorology*, 72, 1445379,  
665 <https://doi.org/10.1080/16000889.2020.1721967>, 2020.
- 666 Axelsson, J., Gao, J., Eckhardt, S., Cassiani, M., Chen, D., and Zhang, Q.: A  
667 Precipitation Isotopic Response in 2014–2015 to Moisture Transport Changes  
668 in the Central Himalayas, *Journal of Geophysical Research: Atmospheres*, 128,  
669 e2023JD038568, <https://doi.org/10.1029/2023JD038568>, 2023.
- 670 Bjerknes, J.: Atmospheric teleconnections from the Equatorial Pacific, *Monthly*  
671 *Weather Review*, 97, 163–172,  
672 [https://doi.org/10.1175/1520-0493\(1969\)097<0163:ATFTEP>2.3.CO;2](https://doi.org/10.1175/1520-0493(1969)097<0163:ATFTEP>2.3.CO;2), 1969.
- 673 Brunello, C. F., Gebhardt, F., Rinke, A., Dütsch, M., Bucci, S., Meyer, H., Mellat, M.,  
674 and Werner, M.: Moisture Transformation in Warm Air Intrusions Into the  
675 Arctic: Process Attribution With Stable Water Isotopes, *Geophysical Research*  
676 *Letters*, 51, e2024GL111013, <https://doi.org/10.1029/2024GL111013>, 2024.
- 677 Cai, Z. and Tian, L.: Atmospheric Controls on Seasonal and Interannual Variations in  
678 the Precipitation Isotope in the East Asian Monsoon Region, *Journal of*  
679 *Climate*, 29, 1339–1352, <https://doi.org/10.1175/JCLI-D-15-0363.1>, 2016.
- 680 Cai, Z., Tian, L., and Bowen, G. J.: ENSO variability reflected in precipitation oxygen  
681 isotopes across the Asian Summer Monsoon region, *Earth and Planetary*  
682 *Science Letters*, 475, 25–33, <https://doi.org/10.1016/j.epsl.2017.06.035>, 2017.
- 683 Chakraborty, S., Sinha, N., Chattopadhyay, R., Sengupta, S., Mohan, P. M., and Datye,  
684 A.: Atmospheric controls on the precipitation isotopes over the Andaman  
685 Islands, Bay of Bengal, *Scientific Reports*, 6, 19555,  
686 <https://doi.org/10.1038/srep19555>, 2016.
- 687 Craig, H.: Isotopic Variations in Meteoric Waters, *Science*, 133, 1702–1703,  
688 <https://doi.org/10.1126/science.133.3465.1702>, 1961.
- 689 Cui, Y., Tian, L., Cai, Z., and Wang, S.: Spatially inhomogeneous response of  
690 precipitation  $\delta^{18}\text{O}$  in China to ENSO cycles, *npj Climate and Atmospheric*  
691 *Science*, 8, 164, <https://doi.org/10.1038/s41612-025-01057-1>, 2025.





- 692 Dai, D., Gao, J., Steen-Larsen, H. C., Yao, T., Ma, Y., Zhu, M., and Li, S.: Continuous  
693 monitoring of the isotopic composition of surface water vapor at Lhasa,  
694 southern Tibetan Plateau, *Atmospheric Research*, 264, 105827,  
695 <https://doi.org/10.1016/j.atmosres.2021.105827>, 2021.
- 696 Dansgaard, W.: Stable isotopes in precipitation, *Tellus*, 16, 436-468,  
697 <https://doi.org/10.1111/j.2153-3490.1964.tb00181.x>, 1964.
- 698 Frankenberg, C., Yoshimura, K., Warneke, T., Aben, I., Butz, A., Deutscher, N.,  
699 Griffith, D., Hase, F., Notholt, J., Schneider, M., Schrijver, H., and Röckmann,  
700 T.: Dynamic Processes Governing Lower-Tropospheric HDO/H<sub>2</sub>O Ratios as  
701 Observed from Space and Ground, *Science*, 325, 1374-1377,  
702 <https://doi.org/10.1126/science.1173791>, 2009.
- 703 Galewsky, J. and Hurley, J. V.: An advection-condensation model for subtropical  
704 water vapor isotopic ratios, *Journal of Geophysical Research: Atmospheres*,  
705 115, <https://doi.org/10.1029/2009JD013651>, 2010.
- 706 Gao, J., He, Y., Masson-Delmotte, V., and Yao, T.: ENSO Effects on Annual  
707 Variations of Summer Precipitation Stable Isotopes in Lhasa, Southern Tibetan  
708 Plateau, *Journal of Climate*, 31, 1173 – 1182,  
709 <https://doi.org/10.1175/JCLI-D-16-0868.1>, 2018.
- 710 Gao, J., Masson-Delmotte, V., Yao, T., Tian, L., Risi, C., and Hoffmann, G.:  
711 Precipitation Water Stable Isotopes in the South Tibetan Plateau: Observations  
712 and Modeling, *Journal of Climate*, 24, 3161-3178,  
713 <https://doi.org/10.1175/2010JCLI3736.1>, 2011.
- 714 Gao, J., Yao, T., Masson-Delmotte, V., Steen-Larsen, H. C., and Wang, W.: Collapsing  
715 glaciers threaten Asia ' s water supplies, *Nature*, 565, 19-21,  
716 <https://doi.org/10.1038/d41586-018-07838-4>, 2019.
- 717 Gao, J., Tian, L., Liu, Y., Gong, T.: Oxygen isotope variation in the water cycle of the  
718 Yamdrok-tso Lake Basin in southern Tibetan Plateau, *Chinese Sci Bull*, 54,  
719 2153-2159, <https://doi.org/10.1007/s11434-009-0487-6>, 2009.
- 720 Gat, J. R.: Oxygen and Hydrogen Isotopes in the Hydrologic Cycle, *Annual Review*



- 721 of Earth and Planetary Sciences, 24, 225-262,  
722 <https://doi.org/10.1146/annurev.earth.24.1.225>, 1996.
- 723 Gat, J. R. and Matsui, E.: Atmospheric water balance in the Amazon basin: An  
724 isotopic evapotranspiration model, *Journal of Geophysical Research:*  
725 *Atmospheres*, 96, 13179-13188, <https://doi.org/10.1029/91JD00054>, 1991.
- 726 Jasechko, S.: Global Isotope Hydrogeology — Review, *Reviews of Geophysics*, 57,  
727 835-965, <https://doi.org/10.1029/2018RG000627>, 2019.
- 728 Gao J., Masson-Delmotte, V., Risi C., He Y., and Yao, T.: What controls precipitation  
729  $\delta^{18}\text{O}$  in the southern Tibetan Plateau at seasonal and intra-seasonal scales? A  
730 case study at Lhasa and Nyalam, *Tellus B: Chemical and Physical*  
731 *Meteorology*, 65, 1,21034, <https://doi.org/10.3402/tellusb.v65i0.21043>, 2013.
- 732 Hersbach, H., Bell, B., Berrisford, P., Biavati, G., Horányi, A., Muñoz Sabater, J.,  
733 Nicolas, J., Peubey, C., Radu, R., Rozum, I., Schepers, D., Simmons, A., Soci,  
734 C., Dee, D., Thépaut, J-N.: ERA5 hourly data on pressure levels from 1940 to  
735 present. Copernicus Climate Change Service (C3S) Climate Data Store (CDS)  
736 [data set], <https://doi.org/10.24381/cds.bd0915c6>, 2023
- 737 Li, J., Tian, L., Xiao, X., and Zhang, C.: Controls on daily to interannual variations of  
738 summer precipitation isotopic signatures from Qinghai Lake watershed,  
739 northeastern Tibetan Plateau, *Theoretical and Applied Climatology*, 152,  
740 1019-1029, <https://doi.org/10.1007/s00704-023-04390-8>, 2023.
- 741 Liu, M., Ren, H., Wang, R., Ma, J., and Mao, X.: Distinct Impacts of Two Types of  
742 Developing El Niño – Southern Oscillations on Tibetan Plateau Summer  
743 Precipitation, *Remote Sensing*, 15, 4030, <https://doi.org/10.3390/rs15164030>,  
744 2023.
- 745 Mason, S. J. and Goddard, L.: Probabilistic Precipitation Anomalies Associated with  
746 ENSO, *Bulletin of the American Meteorological Society*, 82, 619-638,  
747 [https://doi.org/10.1175/1520-0477\(2001\)082<0619:PPAAWE>2.3.CO;2](https://doi.org/10.1175/1520-0477(2001)082<0619:PPAAWE>2.3.CO;2),  
748 2001.
- 749 Merlivat, L. and Jouzel, J.: Global climatic interpretation of the deuterium-oxygen 18



- 750 relationship for precipitation, *Journal of Geophysical Research Atmospheres*,  
751 84, 5029-5033, <https://doi.org/10.1029/JC084iC08p05029>, 1979.
- 752 Murray, N. K., Conroy, J. L., Colin, P. L., Cobb, K. M., and Noone, D. C.: Western  
753 Pacific Warm Pool  $\delta^{18}\text{O}$  Response to the El Niño-Southern Oscillation,  
754 *Geophysical Research Letters*, 52, e2024GL113366,  
755 <https://doi.org/10.1029/2024GL113366>, 2025.
- 756 Natali, S., Doveri, M., Giannecchini, R., Baneschi, I., and Zanchetta, G.: Is the  
757 deuterium excess in precipitation a reliable tracer of moisture sources and  
758 water resources fate in the western Mediterranean? New insights from Apuan  
759 Alps (Italy), *Journal of Hydrology*, 614, 128497,  
760 <https://doi.org/10.1016/j.jhydrol.2022.128497>, 2022.
- 761 Noone, D., Galewsky, J., Sharp, Z. D., Worden, J., Barnes, J., Baer, D., Bailey, A.,  
762 Brown, D. P., Christensen, L., Crosson, E., Dong, F., Hurley, J. V., Johnson, L.  
763 R., Strong, M., Toohey, D., Van Pelt, A., and Wright, J. S.: Properties of air  
764 mass mixing and humidity in the subtropics from measurements of the D/H  
765 isotope ratio of water vapor at the Mauna Loa Observatory, *Journal of*  
766 *Geophysical Research: Atmospheres*, 116,  
767 <https://doi.org/10.1029/2011JD015773>, 2011.
- 768 Risi, C., Bony, S., and Vimeux, F.: Influence of convective processes on the isotopic  
769 composition ( $\delta^{18}\text{O}$  and  $\delta\text{D}$ ) of precipitation and water vapor in the tropics: 2.  
770 Physical interpretation of the amount effect, *Journal of Geophysical Research:*  
771 *Atmospheres*, 113, <https://doi.org/10.1029/2008JD009943>, 2008.
- 772 Risi, C., Bony, S., Vimeux, F., Frankenberg, C., Noone, D., and Worden, J.:  
773 Understanding the Sahelian water budget through the isotopic composition of  
774 water vapor and precipitation, *Journal of Geophysical Research: Atmospheres*,  
775 115, <https://doi.org/10.1029/2010JD014690>, 2010.
- 776 Tian, L., Yao, T., MacClune, K., White, J. W. C., Schilla, A., Vaughn, B., Vachon, R.,  
777 and Ichiyanagi, K.: Stable isotopic variations in west China: A consideration  
778 of moisture sources, *Journal of Geophysical Research: Atmospheres*, 112,



- 779 <https://doi.org/10.1029/2006JD007718>, 2007.
- 780 Tian, L., Cai, Z., Shao, L., Wang, D., and Liu, F.: Review on the study of climatic  
781 significance of precipitation isotope in Asian monsoon region, *Quaternary*  
782 *Sciences*, 41, 856 – 863, <https://doi.org/10.11928/j.issn.1001-7410.2021.03.19>,  
783 2021.
- 784 Wang, R., Ren, H., Liu, M., Zhou, F., and Du, J.: Impact of the central-Pacific ENSO  
785 on the Tibetan Plateau precipitation in boreal spring, *Environmental Research*  
786 *Communications*, 6, 101008, <https://doi.org/10.1088/2515-7620/ad810d>,  
787 2024a.
- 788 Wang, S., Zhang, M., Che, Y., Zhu, X., and Liu, X.: Influence of Below-Cloud  
789 Evaporation on Deuterium Excess in Precipitation of Arid Central Asia and Its  
790 Meteorological Controls, *Journal of Hydrometeorology*, 17, 1973-1984,  
791 <https://doi.org/10.1175/JHM-D-15-0203.1>, 2016.
- 792 Wang, S., Wang, L., Yang, G., Xiao, Y., Argiriou, A. A., Shi, Y., Lei, S., and Zhang,  
793 M.: Altitude effect of precipitation isotopes in an arid mountain-basin system:  
794 Observation and modelling around the world's second-largest shifting desert,  
795 *Journal of Hydrology*, 636, 131351,  
796 <https://doi.org/10.1016/j.jhydrol.2024.131351>, 2024b.
- 797 Wang Y., Yu W., Zhang Y., Zhang T., Gao H., and Muhammad A. W.: Precipitation  
798 stable isotope variation and its relationship with moisture sources in Bagrot  
799 Valley of Upper Indus Basin, *Arid Land Geography*, 42, 252-262,  
800 <https://doi.org/10.12118/j.issn.1000-6060.2019.02.04>, 2019.
- 801 Ren W., Yao T., Yang X., and Joswiak D. R.: Implications of variations in  $\delta^{18}\text{O}$  and  $\delta\text{D}$   
802 in precipitation at Madoi in the eastern Tibetan Plateau, *Quaternary*  
803 *International*, 313 – 314, 56-61, <https://doi.org/10.1016/j.quaint.2013.05.026>,  
804 2013.
- 805 Yang, N. and Wang, G.: Spatial variation of water stable isotopes of multiple rivers in  
806 southeastern Qaidam Basin, northeast Qinghai-Tibetan Plateau: Insights into



- 807 hydrologic cycle, *Journal of Hydrology*, 628, 130464,  
808 <https://doi.org/10.1016/j.jhydrol.2023.130464>, 2024.
- 809 Yang, X., Yao, T., Deji, Zhao, H., and Xu, B.: Possible ENSO Influences on the  
810 Northwestern Tibetan Plateau Revealed by Annually Resolved Ice Core  
811 Records, *Journal of Geophysical Research: Atmospheres*, 123, 3857-3870,  
812 <https://doi.org/10.1002/2017JD027755>, 2018.
- 813 Yao, M., Tang, H., Huang, G., and Wu, R.: Interdecadal shifts of ENSO influences on  
814 Spring Central Asian precipitation, *npj Climate and Atmospheric Science*, 7,  
815 194, <https://doi.org/10.1038/s41612-024-00742-x>, 2024.
- 816 Yao, T., Xie, Z., Wu, X., and Thompson L. G.: Climatic Change Since Little Ice Age  
817 Recorded by Dunde Ice Cap, *Science in China Series B-Chemistry, Life*  
818 *Sciences and Earth Sciences*, 34, 760-767,  
819 <https://doi.org/10.1360/yb1991-34-6-760>, 1991.
- 820 Yao, T., Masson-Delmotte, V., Gao, J., Yu, W., Yang, X., Risi, C., Sturm, C., Werner,  
821 M., Zhao, H., He, Y., Ren, W., Tian, L., Shi, C., and Hou, S.: A review of  
822 climatic controls on  $\delta^{18}\text{O}$  in precipitation over the Tibetan Plateau:  
823 Observations and simulations, *Reviews of Geophysics*, 51, 525 – 548,  
824 <https://doi.org/10.1002/rog.20023>, 2013.
- 825 Yao, T., Thompson, L., Yang, W., Yu, W., Gao, Y., Guo, X., Yang, X., Duan, K., Zhao,  
826 H., Xu, B., Pu, J., Lu, A., Xiang, Y., Kattel, D. B., and Joswiak, D.: Different  
827 glacier status with atmospheric circulations in Tibetan Plateau and  
828 surroundings, *Nature Climate Change*, 2, 663-667,  
829 <https://doi.org/10.1038/nclimate1580>, 2012.
- 830 Ye, L., Zhu, G., Chen, L., Qiu, D., Jiao, Y., Li, R., Lu, S., and Yang, J.: Influence of  
831 below-cloud evaporation on stable isotopes of precipitation in the Yellow  
832 River source region, *Hydrological Processes*, 38, e15064,  
833 <https://doi.org/10.1002/hyp.15064>, 2024.
- 834 Yoshimura, K.: Stable Water Isotopes in Climatology, Meteorology, and Hydrology: A  
835 Review, *Journal of the Meteorological Society of Japan. Ser. II*, 93, 513-533,



- 836 10.2151/jmsj.2015-036, 2015.
- 837 Yoshimura, K., Kanamitsu, M., Noone, D., and Oki, T.: Historical isotope simulation  
838 using Reanalysis atmospheric data, *Journal of Geophysical Research:*  
839 *Atmospheres*, 113, <https://doi.org/10.1029/2008JD010074>, 2008.
- 840 Yu, W., Ma, Y., Sun, W., Wang, Y.: Climatic significance of  $\delta^{18}\text{O}$  records from  
841 precipitation on the western Tibetan Plateau, *Chinese Sci Bull*, 54, 2131-2139,  
842 <https://doi.org/10.1007/s11434-009-0495-6>, 2009.
- 843 Zhang, F., Huang, T., Man, W., Hu, H., Long, Y., Li, Z., and Pang, Z.: Contribution of  
844 Recycled Moisture to Precipitation: A Modified D-Excess-Based Model,  
845 *Geophysical Research Letters*, 48, e2021GL095909,  
846 <https://doi.org/10.1029/2021GL095909>, 2021.
- 847 Zhang, J., Yu, W., Lewis, S., Thompson, L. G., Bowen, G. J., Yoshimura, K.,  
848 Cauquoin, A., Werner, M., Chakraborty, S., Jing, Z., Ma, Y., Guo, X., Xu, B.,  
849 Wu, G., Guo, R., and Qu, D.: Controls on Stable Water Isotopes in Monsoonal  
850 Precipitation Across the Bay of Bengal: Atmosphere and Surface Analysis,  
851 *Geophysical Research Letters*, 50, e2022GL102229,  
852 <https://doi.org/10.1029/2022GL102229>, 2023.